Multiphase flow modeling in centrifugal partition chromatography

S. Adelmann, C. Schwienheer, G. Schembecker*

Laboratory of Plant and Process Design, Department of Biochemical and Chemical Engineering, Technische Universität Dortmund, Emil-Figge-Str. 70, 44221 Dortmund, Germany

ABSTRACT

The separation efficiency in Centrifugal Partition Chromatography (CPC) depends on selection of a suitable biphasic solvent system (distribution ratio, selectivity factor, sample solubility) and is influenced by hydrodynamics in the chambers. Especially the stationary phase retention, the interfacial area for mass transfer and the flow pattern (backmixing) are important parameters. Their relationship with physical properties, operating parameters and chamber geometry is not completely understood and predictions are hardly possible. Experimental flow visualization is expensive and two-dimensional only. Therefore we simulated the flow pattern using a volume-of-fluid (VOF) method, which was implemented in OpenFOAM®. For the three-dimensional simulation of a rotating FCPC®-chamber, gravitational centrifugal and Coriolis forces were added to the conservation equation. For experimental validation the flow pattern of different solvent systems was visualized with an optical measurement system. The amount of mobile phase in a chamber was calculated from gray scale values of videos recorded by an image processing routine in ImageJ®. To visualize the flow of the stationary phase polyethylene particles were used to perform a qualitative particle image velocimetry (PIV) analysis. We found a good agreement between flow patterns and velocity profiles of experiments and simulations. By using the model we found that increasing the chamber depth leads to higher specific interfacial area. Additionally a circular flow in the stationary phase was identified that lowers the interfacial area because it pushes the jet of mobile phase to the chamber wall. The Coriolis force alone gives the impulse for this behavior. As a result the model is easier to handle than experiments and allows 3D prediction of hydrodynamics in the chamber. Additionally it can be used for optimizing geometry and operating parameters for given physical properties of solvent systems.

© 2011 Elsevier B.V. All rights reserved.

1. Introduction

Centrifugal Partition Chromatography (CPC) is widely used for the (semi-)preparative separation of natural products. The separation is based on the partition between the phases of a biphasic liquid system. The unique feature of CPC is the lack of any kind of solid support because mobile and stationary phases are liquids. The retention of the stationary phase results from applying a centrifugal force field and its liquid character allows changing mobile and stationary phase during a separation by switching the flow direction. The liquid nature of the stationary phase leads to many different modes of operation besides the classical elution in ascending or descending mode [1,2].

However, as well as the selection of a suitable solvent system with a sufficient distribution ratio of the target compound(s), the separation efficiency is strongly affected by the hydrodynamics in the chambers that are connected by ducts. Up to now the dependency of the hydrodynamics on operating parameters (e.g. volume flow, rotational speed) and physical properties (e.g. densities, interfacial tension) is not completely understood.

Flow visualization, first accomplished by van Buel et al. [3], enhanced the knowledge of flow behavior in CPC cells. The first visualization of the Coriolis effect in CPC cells by Marchal et al. [4,5] improved the understanding of flow pattern and its influence on resolution. His work also had significant impact on the chamber geometry development of CPC cells. Additionally he proved that greater rotational speeds enhanced resolution due to smaller droplets and increased mass transfer between the phases. Higher volume flows in certain ranges also enhanced the resolution. In a recent paper [6] we showed that important hydrodynamic parameters such as interfacial area for mass transfer, stationary phase retention and the distribution of the mobile phase were strongly dependent on operating parameters and physical properties of the solvent system. But all experiments on the hydrodynamics were performed in different CPC devices, for different phase systems and

thus are hardly comparable or transferable. So there is still a lack of knowledge and the selection of suitable operating parameters for different phase systems and chamber geometries is mostly driven by the experience of the chromatographer or trial and error.

The prediction of flow patterns by computational fluid dynamics (CFD) therefore has an important role in the design and operation of CPC instrumentation. Up to now no CFD calculation of biphasic flow patterns in CPC chambers is known to the authors. The only CFD calculations in that area were performed with a 2D homogenous two fluid model for a Counter Current Chromatography (CCC) device [7]. Instead of chambers and ducts that rotate around a single axis a CCC device consists of coiled tubing that undergoes planetary motion [8].

In our study a 3D volume-of-fluid (VOF) method was chosen for the calculation of the two-phase flow pattern in a CPC chamber. The only input parameters of this method are physical properties of the solvent system and operating parameters. No empirical correlation functions have to be used in the model. For its validation we compared simulated and experimental flow patterns and interfacial area. Additionally we performed a qualitative particle image velocimetry (PIV) analysis for the experimental proof of the circular flow of the stationary phase predicted by the CFD model.

2. Experimental and image processing

The optical measurement system enables images of the flow pattern in a CPC chamber to be taken. A red flash LED was used for transmitted light illumination. Additionally a selective soluble dye methylene blue (soluble in the lower mobile phase) with a high extinction for the illumination wavelength was dissolved in the phase system to enhance the contrast between the phases. From the two-dimensional images the mobile phase thickness and the interfacial area between the phases were calculated. The set-up of the transparent rotor, video instrumentation, experimental and the complete calculation procedure, for the flow videos in hydrodynamic equilibrium, was described elsewhere [6]. The hydrodynamic equilibrium, when only mobile phase leaves the rotor, was reached after pumping the mobile phase for 2–10 min. For validation of the CFD model additionally a qualitative particle image velocimetry (PIV) analysis was performed and inflow videos were taken. As a result the set-up of the optical measurement system, the experimental procedures and the image processing routines had to be adjusted.

2.1. PIV analysis

Particle image velocimetry (PIV) analysis is an experimental method to measure velocities and flow directions in fluids. Marker particles are inserted into the fluid and two images are taken within a small period of time Δt. The marker particle should be able to follow the fluid flow without disturbing it. Thus the particles should be very small, spherical, of equal size and the density should be close to that of the surrounding fluid. Additionally only one layer, perpendicular to the main flow direction, should be illuminated or focused. The direction and velocity of a marker particle is afterwards calculated by its positions in the first and second image and the period Δt between taking the images [9].

For the PIV analysis a high speed camera (High Speed Star 3, La Vision) and a self-made rotor plate was used. For a resolution of 950×527 pixels the camera allowed to take up to 1500 images per second. For manufacturing the so-called PIV rotor we measured the chamber geometry of an original FCPC® rotor plate with a microscope. The rotor was afterwards manufactured by laser cutting (Wiegand GmbH) and had six sections with four chambers connected in series as shown in Fig. 1. The PIV-rotor was assem-
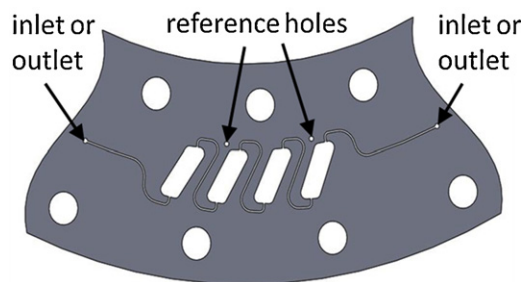

Fig. 1. Section of PIV-rotor with reference holes with a chamber depth of 2.5 mm and a duct width of 0.28 mm (other dimensions similar to regular FCPC® chamber).

bled analogous to the transparent rotor in [6]. Using four chambers connected in series only made it much easier to insert the particles into the visualized chambers. The rotor depth was 2 mm (instead of 2.5 mm for the original FCPC®) and it was equipped with drilled reference holes (see Fig. 1) that were used for adjusting the image positions due to the rotation.

The marker particles were ultra high molecular weight polyethylene particles (GUR® UHMWPE, Ticona). Their size varied between 63 and 125 μm and their shape was irregular. The particle density was about 930 kg/m³ and was thus between upper and lower phase of the ethyl acetate/water system ($\rho_{\mathrm{up}} = 892.8$ kg/m³, $\rho_{\mathrm{lo}} = 996.3$ kg/m³). As the experimental set-up does not allow illuminating or focusing only one layer of the chamber the results of the PIV analysis have to be regarded as qualitatively.

In order to distinguish between mobile and stationary phase the mobile phase was dyed with a small amount of methylene blue (10 mg per liter of mobile phase). The extinction of the solid marker particles was much higher. As the particles stuck together in the mobile phase, these had to be inserted into the chamber with the stationary phase. Therefore a small amount of particles was added to 10 ml of stationary phase and put into a 10 ml sample loop. After filling the rotor with stationary phase the content of the sample loop was pumped at a high volume flow (30 ml/min) and a low rotational speed (500 rev/min) into the rotor. This was done in ascending mode to keep as many particles in the chambers as possible. Then the inlet tubing of the rotor was unscrewed and dyed mobile phase without particles was pumped until all the stationary phase left the tubing. The inlet tubing was screwed into the rotor again and the rotation was set to the desired speed. Then mobile phase was pumped into the rotor at a particular volume flow. The image grabbing (7000 images) was started directly after activating the pump.

Only serial image pairs that showed both reference holes were used for the analysis and all other images were dismissed. The second image of these image pairs was rotated and moved so that the reference holes in both images were at the same position. The analysis by cross correlation techniques to evaluate the particle velocity gave no reasonable results because the particles could hardly be identified by the software in both images. The reason was the varying flow direction of the particles and their different velocities because of size and unknown distance to the wall in z-direction. Additionally the large rotation of the second image made an interpolation necessary that blurred the particle shape. As a result the particles that were the same in both images had to be identified manually. The position of each clearly identified particle was then measured manually in ImageJ® by tagging the x and y coordinates of a specific edge of a particle in both images. With the period $\Delta t = 0.667$ ms between taking the images the absolute velocity and flow direction of a particle were calculated.

The density difference between particles and fluids causes different velocities. For the assumption of ideal spherical particles the relative velocity v_{rel} between a particle with the diameter d_{p} and

the stationary phase can be derived from the balance of particle weight, buoyancy and friction [10]:

$$v_{rel} = \sqrt{\frac{4 \cdot \vec{a} \cdot d_p \cdot (\rho_p - \rho_s)}{3 \cdot \rho_s \cdot (24/Re + 4/\sqrt{Re} + 0.4)}} \tag{1}$$

where $Re = v_{rel} \cdot d_p \cdot \rho_s / \eta_s$ is the Reynolds number, η_s is the viscosity of the stationary phase and ρ is the density. For the ethyl acetate/water solvent system (properties see Table 3 in Section 4.3), a mean particle diameter of 94 μm and a centrifugal acceleration $\bar{a}$ of 2257 m/s^2 (1400 rev/min for a rotational radius of 0.105 m) the relative velocity is 0.056 m/s. The relative velocity varies in the range of 0.021–0.109 m/s for rotational speeds between 1000 and 1800 rev/min and (spherical) particle diameters between 63 and 125 μm. Coriolis acceleration and the irregular shape were neglected for this calculation. As the mean and maximal velocities of particles were measured in the range of 0.1 and 0.2 m/s and 0.3–0.8 m/s respectively the relative velocities have to be considered for the interpretation.

2.2. Filling process of the chambers

The PIV-rotor was also used for taking the so-called inflow video to visualize the filling process in a chamber. Therefore the rotor was filled with stationary phase and a so-called blank video was taken which contains stationary phase only. Then the dyed mobile phase was pumped into the rotor and the inflow video was recorded. The methylene blue concentration was 30 mg/l in the mobile phase. The calculation of mobile phase thickness was done analogous to the procedure given in [6].

2.3. Chemicals

Ethyl acetate (99.9%) was purchased from Carl Roth GmbH + Co KG and the water used was demineralized. The water free polar dye methylene blue (dye content >82%) was from Merck KGaA and the sieve fraction of marker particles was sent to us by Ticona.

3. Numerical model

In our study we developed a 3D computational fluid dynamics (CFD) model for the biphasic flow in a FCPC® chamber. For solving the conversion equations the "InterFOAM"-solver was used that is implemented in OpenFOAM (Open Field Operation And Manipulation) [11]. The solver is based on the volume-of-fluid (VOF) method after Hirt and Nichols [12] and the discretization is done by the finite volume method.

The balance for an infinitesimal volume element for an incompressible, Newtonian fluid with constant density ρ and viscosity η, the unknown velocity components $\vec{U}$ and the unknown pressure p as functions of the coordinates x, y, z, and the time t is given by [13]

$$\rho \cdot \left(\frac{\partial \vec{U}}{\partial t} + \vec{U} \cdot \nabla \vec{U} \right) = -\nabla p + \eta \cdot \Delta \vec{U} + \rho \cdot \vec{\phi} \tag{2}$$

$$\nabla \vec{U} = 0$$

where $\vec{\phi}$ stands for the mass-specific force vector (dimensionally, an acceleration) due to body forces like the gravitational force, ∇ is the Del operator and Δ is the Laplace operator. A numerical solution is needed to solve this system of four differential equations. For the simulation of the biphasic flow in a CPC chamber the position of the interface of the fluids has to be known for the calculation of the resulting properties and the surface force (see Section 3.1). The additional body forces have to be implemented (see Section 3.2), the calculation domain has to be discretized locally and temporally

(see Section 3.3) and initial and boundary conditions have to be defined (see Section 3.4).

3.1. VOF method

In the VOF method both fluids are combined to one surrogate fluid. For the phase differentiation an indicator function α, defined by the ratio of the volume of phase 1 in a grid cell and the grid cell volume, is used. For pure phase 1 (the lower phase) α has the value one and for phase 2 (the upper phase) the value is zero. As α has to be a continuous function, α is between zero and one in the interfacial area. For the time and space evolution of α an additional transport equation is needed:

$$\frac{\partial \alpha}{\partial t} + \nabla(\vec{U} \cdot \alpha) + \nabla(\vec{U}_r \cdot \alpha \cdot (1 - \alpha)) = 0 \tag{3}$$

The equation describes the convective transport of α as a function of the velocity $\vec{U}$. The additional term $\nabla(\vec{U}_r \cdot \alpha \cdot (1 - \alpha))$ is used for an artificial compression of the interfacial area where α is between zero and one. The velocity $\vec{U}_r$ stands for appropriate velocity [14]. The gradient of α equals a surface vector normal to the surface whose norm equals the interfacial area and is also used for calculation of the volumetric interfacial forces $\vec{f}_{sf}$ with the continuous surface model (CSF) by Brackbill et al. [15]:

$$\vec{f}_{sf} = \sigma \cdot \kappa \cdot \nabla \alpha \tag{4}$$

where σ is the interfacial tension, κ is the curvature of the interfacial area that is given by

$$\kappa = \nabla \left(\frac{\nabla \alpha}{|\nabla \alpha|} \right) \tag{5}$$

where $\nabla \alpha$ is the gradient of the indicator function. The density ρ and viscosity η are calculated by the mixing rules $\rho = \alpha \cdot \rho_1 + (1 - \alpha) \cdot \rho_2$ and $\eta = \alpha \cdot \eta_1 + (1 - \alpha) \cdot \eta_2$.

3.2. Implementation of centrifugal, Coriolis and gravity forces

Besides the volumetric interfacial forces $\vec{f}_{sf}$ the mass-specific forces due to centrifugal, Coriolis and gravitational acceleration had to be included into the conservation equation. For a counterclockwise rotation of the chamber with the rotational speed f around the z-axis, the angular speed is given by $\vec{\omega} = (0 \ \ 0 \ \ \omega_z)$ with $\omega_z = 2 \cdot \pi \cdot f$. The resulting mass-specific forces or accelerations respectively in a fixed grid are given by

$$\vec{\phi}_{ce/Co/gr} = \begin{pmatrix} R_{x,gc} \cdot \omega_z^2 \\ R_{y,gc} \cdot \omega_z^2 \\ 0 \end{pmatrix} + \begin{pmatrix} 2 \cdot (U_{y,gc} \cdot \omega_z) \\ -2 \cdot (U_{x,gc} \cdot \omega_z) \\ 0 \end{pmatrix} + \begin{pmatrix} 0 \\ 0 \\ -g \end{pmatrix} \tag{6}$$

where $\vec{R}_{gc} = (R_{x,gc} \ \ R_{y,gc} \ \ 0)$ is the vector between rotation axis and center of the grid cell and g is the gravitational acceleration. Besides the continuity equation $\nabla \vec{U} = 0$ the resulting conversion equations that have to be solved for the simulation of a biphasic flow are

$$\rho \cdot \left(\frac{\partial \vec{U}}{\partial t} + \vec{U} \cdot \nabla \vec{U} \right) = -\nabla p + \eta \cdot \Delta \vec{U} + \sigma \cdot \kappa \cdot \nabla \alpha + \rho \cdot \phi_{ce/Co/gr} \tag{7}$$

In the simulation the constant centrifugal acceleration was calculated for each grid cell at the beginning of the calculation. The velocity dependent Coriolis acceleration was calculated for each time step from the velocities or the previous one.

3.3. Local and time discretization

For the finite volume method the spacial domain had to be discretized by using a numerical grid with a finite number of cells. As we used two different chamber geometries in the experiments we

Table 1
Dimension of grids for the simulations used and corresponding chamber of experiments.

	Unit	Grid A	Grid B
Distance of rotation axis and center of the chamber	[mm]	105.15	105.5
Duct width (inlet and outlet)	[mm]	0.35	0.28
Chamber depth	[mm]	2.5	2.0
Chamber width (normal to long chamber edges)	[mm]	4.34	4.34
Chamber length (distance of inlet and outlet)	[mm]	10.8	10.8
Corresponding chamber geometry of experiments		Chamber of regular FCPC®	Chamber of PIV-rotor
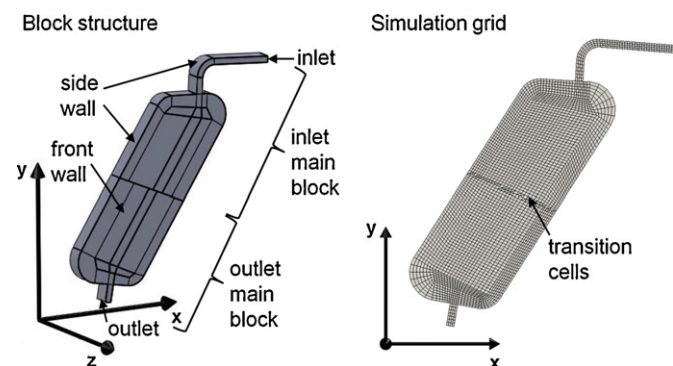
Fig. 2. Block structure with main blocks and naming of lateral faces (left) – block structure similar for all grids is used, simulation grid with 3568 cells in xy-plane (right).

had to define two different grids. The parameters of those grids are shown in Table 1. The resolution of grids in the simulations used is given in the caption of the corresponding figure.

The block structures of both grids were similar. The structured grids of the simulation domain contained two main blocks. Inlet and outlet main blocks were split into 16 and 14 blocks respectively. The main blocks were connected by transition cells (function in Open-FOAM) that allowed the connection of blocks although the number of cells at their neighboring surface was unequal. The grid with the lowest resolution in the xy-plane and the blocking structure with all surfaces are shown in Fig. 2. Different grid resolutions for grid A were used for the estimation of the minimum local discretization (see Section 3.5).

The time discretization for all simulations was done by adjusting the time step size δt. For this purpose the Courant criterion with the Courant number

$$Co = \frac{|\vec{U}| \cdot \delta t}{\delta X_{gc}} \tag{8}$$

was used. In Eq. (8) $\vec{U}$ is the total velocity and δX_{gc} is the dimension of the grid cell in the main flow direction. The time step size was adjusted that in each grid cell the maximum Courant number Co was below 0.5.

3.4. Initial and boundary conditions

For solving the differential conservation equations of the VOF method numerically initial and boundary conditions had to be defined. For initialization the whole chamber was filled with the

Table 2
Initial and boundary conditions for the simulations (velocity $\bar{U}$, pressure p and indicator function α).

Position	$\bar{U}$	p	α
Inlet	$\bar{U}_{in}$	$\triangledown \rho = 0$	1
Outlet	$\nabla \bar{U} = 0$	p_{out}	$\triangledown \alpha = 0$
Side walls	$(0\,0\,0)$	$\triangledown \rho = 0$	$\triangledown \alpha = 0$
Front and back wall	$(0\,0\,0)$	$\triangledown \rho = 0$	0
Initial (whole volume)	$(0\,0\,0)$	0	0

upper stationary phase ($\alpha = 0$). Lower mobile phase ($\alpha = 1$) entered the chamber through the inlet with the velocity $\bar{U}_{in} = \dot{V}_{in}/A_{in}$ that was given by the ratio of volume flow $\dot{V}_{in}$ and cross sectional area of the inlet A_{in}. For the metal surfaces (side walls) the contact angle was set to 90° ($\triangledown \alpha = 0$) and the angle of front and back wall was 180° ($\alpha = 0$) because the hydrophobic FEP-foils were hardly wetted by the lower water rich phase. For all walls the no slip condition ($\vec{U} = (0\ 0\ 0)$) was applied. For a more stable simulation the pressure level at the outlet was set to a constant value p_{out} [16]. All initial and boundary conditions are given in Table 2.

3.5. Estimation of local discretization

In order to reduce calculation time we simulated grid A (2.5 mm depth) with a varying number of grid cells in xy-plane and z-direction for a rotational speed of 1800 rev/min and a volume flow 15 ml/min. The physical properties of ethyl acetate/water solvent system are given in Table 3 (see Section 4.3). For the comparison of the different grid sizes the interfacial area IA was calculated directly from the simulations by

$$IA = \sum_{i=0}^{N_{gc}} |\nabla \alpha_i| \cdot V_{gc,i} \tag{9}$$

where N_{gc} is the total number of grid cells, $\nabla \alpha$ the gradient of the indicator function and $V_{gc,i}$ is the volume of the grid cell i. The time dependent trend of the interfacial area is shown in Fig. 3 for a medium volume flow of 15 ml/min and a high rotational speed of 1800 rev/min. In the left diagram the grid with 16,099 cells in the xy-plane and 30 cells in z-direction shows the highest interfacial area for these operating conditions. For different volume flows and rotational speeds usually the lowest grid counts showed the highest values for the interfacial area. The high dispersion due to the high rotational speed caused some round-off errors of the indicator function. Values below zero and above one are limited to the
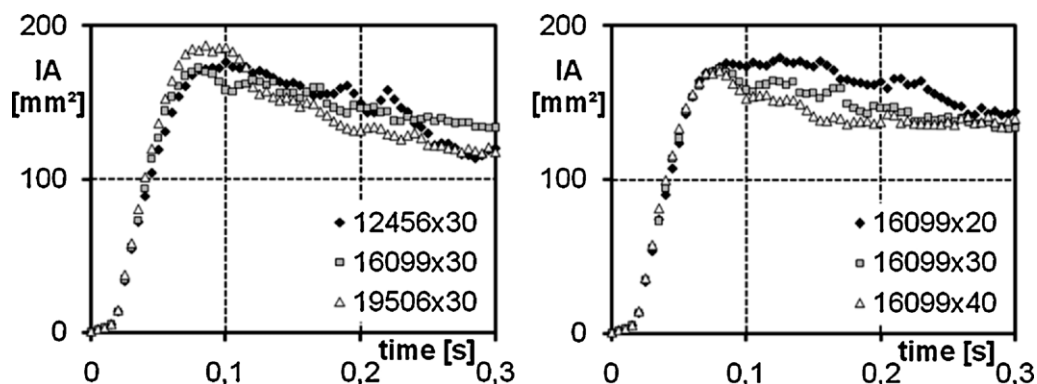
Table 3
Physical properties of original ethyl acetate/water solvent system (values from [6]) and artificially created solvent systems, bold values are adapted (italics indicate the resulting changes).

Used abbreviation	Unit	EtAcWat	Artificial 1	Artificial 2	Artificial 3	Artificial 4	Artificial 5	Artificial 6
Density difference $\triangledown \rho$	kg/m³	103.5	10.35	103.5	*51.75*	*155.75*	103.5	103.5
Density ρ_{lo}	kg/m³	996.3	996.3	996.3	**944.55**	**1048.55**	996.3	996.3
Interfacial tension σ	mN/m³	6.45	**2.45**	**10.425**	6.45	6.45	6.45	6.45
Dyn. viscosity η_{up}	mPa s	0.47	0.47	0.47	0.47	0.47	**0.47**	0.47
Dyn. viscosity η_{lo}	mPa s	1.07	1.07	1.07	1.07	1.07	0.47	**4.70**
Parameter $\sigma/\Delta\rho$	s²/cm³	62.3	*23.7*	*101.1*	*124.6*	*41.4*	62.3	62.3

Fig. 3. Interfacial area IA for grid A with different numbers of cells in *xy*-plane and *z*-direction, rotational speed is 1800 rev/min and volume flow is 15 ml/min (EtAcWat system, descending mode); cells in *xy*-plane varied and constant in *z*-direction (left), cells in *z*-direction varied and constant in *xy*-plane (right).

physical boundaries of zero and one. This caused mass discontinuities and the decrease of the interfacial area for the grid with 12,456 cells in the *xy*-plane. This behavior was also seen for the grid with 19,506 cells. The problem in this grid was the comparably low resolution in the *z*-direction of 30 cells. The resulting hexahedron grid cells were farther away from the geometry of a cube than the grid with 16,099 cells.

The right diagram of Fig. 3 shows the resulting interfacial area for different cell counts in the *z*-direction and 16,099 cells in the *xy*-plane. The trend of the graphs is similar. The grid with only 20 cells in *z*-direction varies most from the other two. This grid had the lowest resolution in *z*-direction and the cells that were most different to cubic cells. The other two grids showed only small differences and therefore the grid with lower resolution (16,099 × 30) was selected to save computing time.

It has to be mentioned that the suitable grid size is strongly dependent on operating parameters and phase properties because the resulting dispersion and calculated droplet size are affected. The flow pattern does not change much for the different grid sizes investigated especially for low and medium rotational speeds and volume flows. Therefore a medium sized grid with 12,456 cells in *xy*-plane and 20 cells in *z*-direction was also used for saving calculation time. That grid was found sufficient for a rotational speed of 1000 rev/min and a volume flow of 9 ml/min. The calculation of interfacial areas (see Section 4.3) was performed with a higher resolution grid (16,099 × 30).

4. Results and discussion

The results section is divided into three parts. First the velocity profiles of the simulations are compared to the experimental results of the PIV-analysis. In the second part experimental flow patterns are compared to the simulation results in detail and the influence of operating parameters on sheet deflection and dispersion is shown. In the last part the model is used to calculate the effect of chamber depth and different physical properties on the resulting interfacial area between the phases. All experiments were performed for the descending mode with lower phase mobile.

4.1. Velocity profiles

In the simulations a circulation of the stationary phase was observed. For easier comparison to the experimental results of the PIV analysis the velocities of the simulations were averaged in *z*-direction for each pixel in the *xy*-plane. For the averaging only velocity components in the *x*- and *y*-direction were considered. The resulting average velocities of the simulations are shown in Fig. 4. The arrow size indicates the averaged velocity in the *xy*-plane. In addition the mobile phase fractions of the simulation results were averaged in *z*-direction to obtain a 2D distribution of the mobile phase (mobile phase thickness). For all volume flows the circular flow is observed.

For experimental validation a PIV-analysis was performed in order to visualize the flow of the stationary phase. The resulting flow directions of the particles in the *xy*-plane are shown in Fig. 5 for the same operating parameters as in Fig. 4. The particle velocity, which is indicated by the arrow size, does not equal the real phase velocities because of the density difference between fluid and particle (see Eq. (1)). Additionally the position of a particle in the *z*-direction was not detectable. Therefore the results are only compared qualitatively.
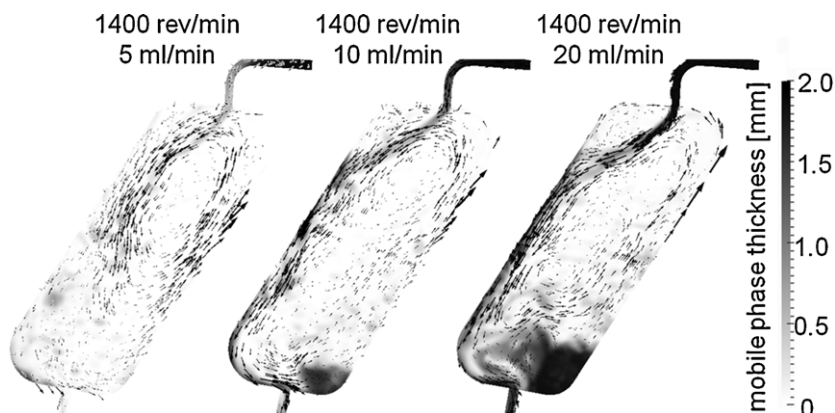

Fig. 4. Simulated flow pattern with averaged velocity profiles of the EtAcWat system, rotational speed is 1400 rev/min and volume flows are 5, 10 and 20 ml/min (from left to right); mobile phase thicknesses are averaged phase fractions in *z*-direction; grid B with 12,456 cells in *xy*-plane and 20 cells in *z*-direction is used.
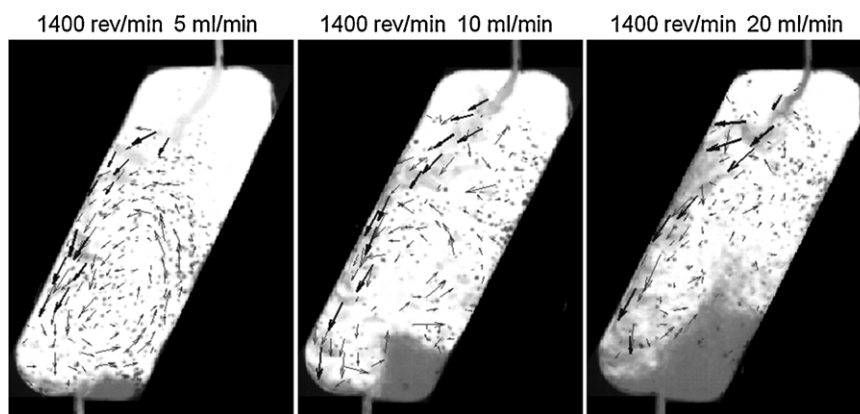
Fig. 5. Raw images of experiments with resulting velocity profiles of the PIV analysis of the EtAcWat system, rotational speed is 1400 rev/min and volume flows are 5, 10 and 20 ml/min (from left to right); arrows show flow directions and arrow size indicates velocity, slender arrows indicate the particle velocity, thick arrows indicate the velocities of the dyed mobile phase, PIV-rotor used.

However, a circulating flow of the stationary phase was visualized clearly for low volume flows. For low volume flows no particles are detected at the upper part of the chamber. This probably results from the density difference of the particles and the stationary phase (see Section 2.1). Therefore the circular flow is observed in the lower part of the chamber in contrast to the simulation results. For a high volume flow of 20 ml/min a greater amount of particles was located in the upper part of the chamber closer to the rotation axis for higher volume flows. This clearly indicates the existence of a strong stationary phase flow towards the upper part of the chamber that was also seen in the simulation results.

The main differences for the different volume flows are the profiles in specific layers of the z-direction. The velocities for different layers in z-direction of grid cells in the xy-plane are shown in Fig. 6. The absolute velocities in z-direction are given by the additional scale. The velocities in the xy-plane for $z = 0.5$ mm and $z = 1.5$ mm are very similar for the low volume flow. For higher volume flows these are totally different. At some chamber positions the flow is directed downwards in one layer in z-direction whereas it is directed in the opposite direction in another layer. Besides higher velocities

in z-direction also the total velocities increase for higher volume flows. This results for low volume flows in small changes of the flow patterns and velocity profiles with time. Higher volume flows lead to unsteady flow patterns with increased dispersion and higher velocities.

4.2. Comparison of experimental and simulated flow pattern

In order to validate the CFD model we compared experimental and simulation results. The 2D flow patterns (phase fractions of simulations averaged in z-direction to obtain the mobile phase thickness) of simulations and experiments with different operating parameters are shown in Fig. 7 for the EtAcWat system. The flow patterns are in good agreement. Besides the similar prediction of mobile phase sheet deflection due to the Coriolis force also the degree of dispersion is comparable. The stronger dispersion in the simulations for the rotational speed of 1800 rev/min is probably the result of the used grid size of 12,456 cells in the xy-plane and 20 cells in z-direction (compare Section 3.5). Generally the experimentally measured flow pattern in a FCPC® was predicted very well by the CFD model.
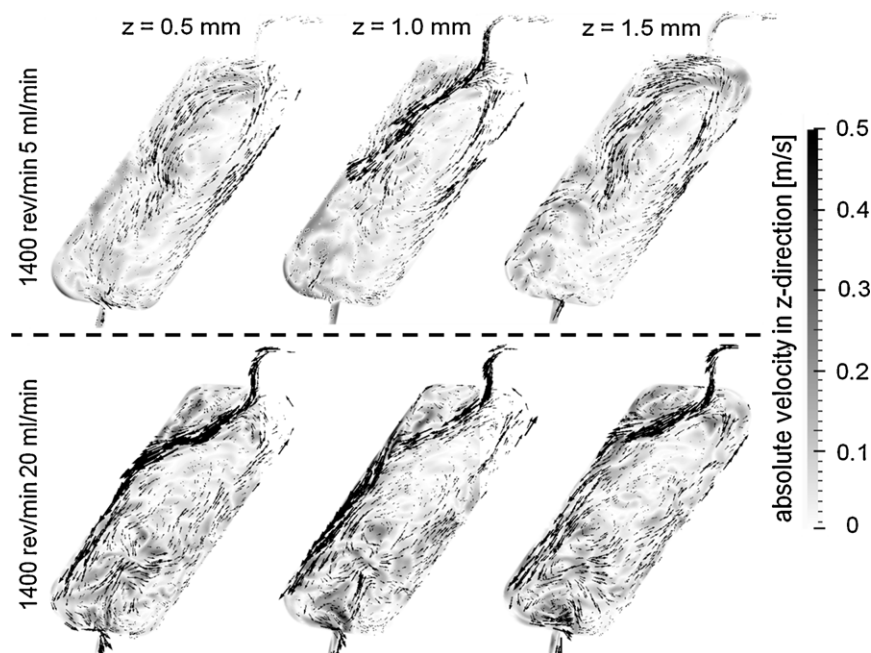

Fig. 6. Velocity profiles and absolute velocities in z-direction for specific z-coordinates 0.5 mm, 1.0 mm and 1.5 mm; arrow size indicates velocity in xy-plane, absolute velocities in z-direction are given in the gray value scale; grid B with 12,456 cells in xy-plane and 20 cells in z-direction is used.
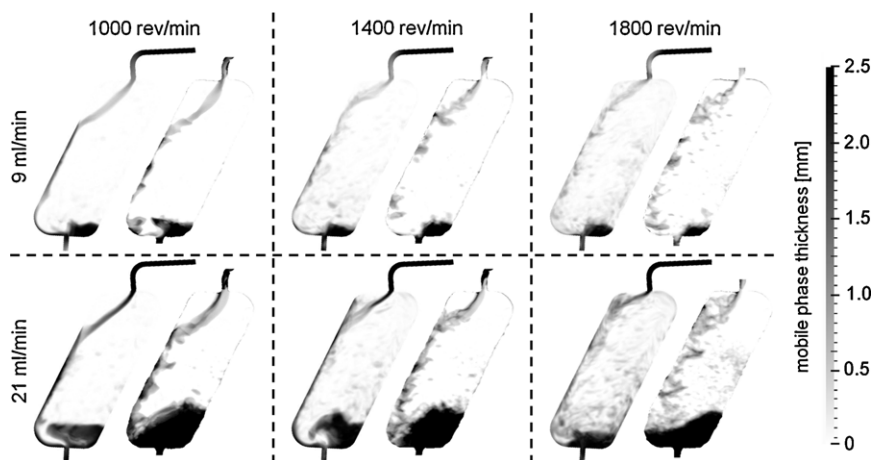
Fig. 7. Comparison of simulated (left of each field) and experimental (right of each field) flow patterns for different rotational speeds and volume flows; grid A (regular FCPC® rotor) with 12,456 cells in xy-plane and 20 cells in z-direction is used; mobile phase thicknesses are averaged phase fraction z-direction; experimental flow pattern is in hydrodynamic equilibrium after the procedure given in [6].

The different stationary phase retention of simulations and experiments in Fig. 7 is the result of different periods of mobile phase flowing into the chamber. With respect to the computing time the simulations were performed for 0.3 s whereas the experimental images were taken in the hydrodynamic equilibrium after 2–10 min pumping of mobile phase (see Section 2 or [6]). Therefore the stationary phase retention of the simulation is always higher than the retention in the experiments. Additionally no coalescence phenomena are implemented in the model.

For comparison of simulations and experiments during the filling process of the chambers we took the inflow videos with the PIV-rotor (see Section 2.2). The image sequences in Fig. 8 show the unsteady filling process of the experimental inflow videos. The flow pattern is more disperse in the beginning and the sheet is less deflected. A small amount of stationary phase from the previous chamber or duct entered the visualized chamber simultaneously with the mobile phase. Thus it took longer to reach a steady state in the experiments. Additionally the stationary phase in the chamber did not move in the beginning. Pumping in the mobile phase caused the stationary phase to accelerate due to the drag at the interfacial area. After a short period of time a circular flow of the stationary phase established in the chamber. It lowers the relative velocity between the phases, reduces the drag force on the mobile phase and decreases the sheet break-up after a certain time.

For the lower rotational speed and the smaller volume flow the sheet of mobile phase became steady and did not change the direction any more. The image sequences of 1000 rev/min – 15 ml/min and 1400 rev/min also show that the sheet of mobile phase does not change the direction and the sheet break-up occurs at the same position. For 1400 rev/min – 15 ml/min the sheet was
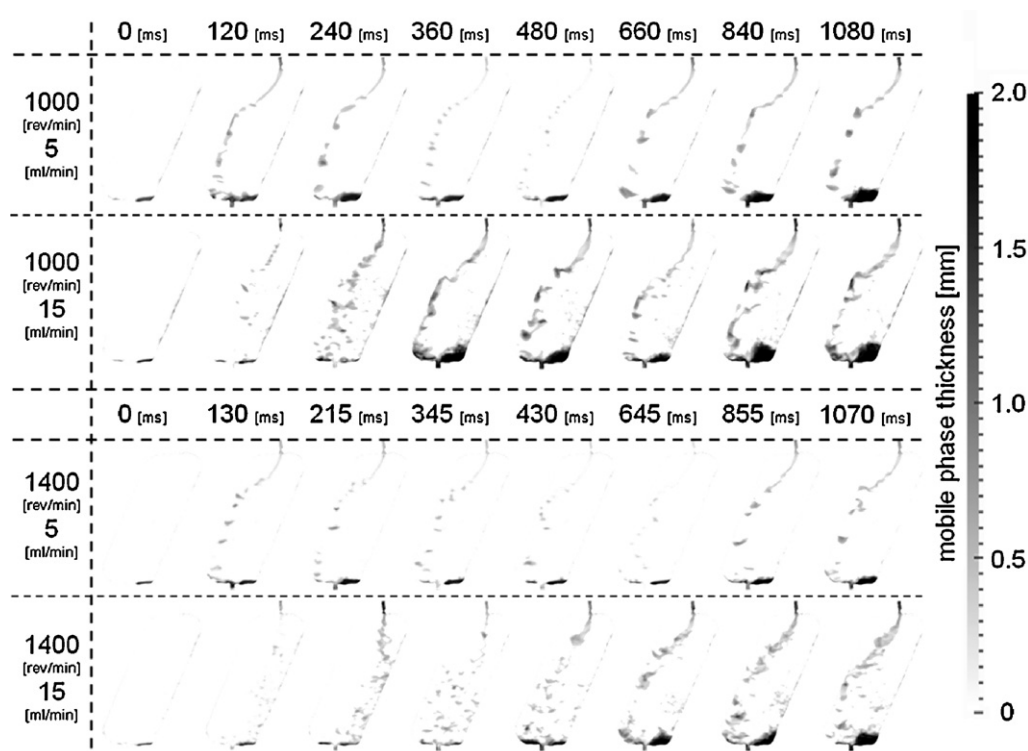

Fig. 8. Image sequences with mobile phase thicknesses of experimental inflow videos (filling process) for different times, rotational speeds and volume flows (PIV-rotor).
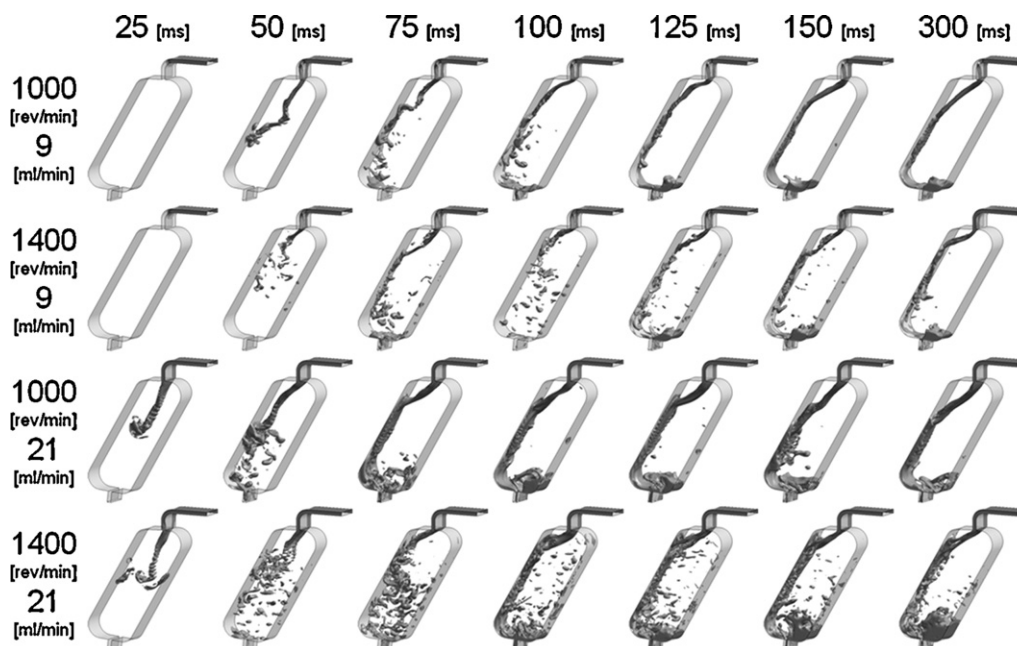
Fig. 9. 3D-plots of mobile phase flow (iso-surfaces with indicator function value $\alpha = 0.5$) for volume flows of 9 and 21 ml/min, rotational speeds of 1000 and 1400 rev/min and different times of the simulation (25, 50, 75, 100, 125, 150 and 300 ms) in the EtAcWat system; grid A with 12,456 cells in xy-plane and 20 cells in z-direction is used.

not deflected at all in the beginning. Additionally the sheet keeps changing its direction and break-up occurs at various positions and sheet lengths.

The filling process of simulations and experiments was slightly different. In the simulations the mobile phase fraction at the inlet was set to 1 via boundary condition. Thus the flow became steady earlier and the interfacial area IA was nearly constant after 0.3 s (see Section 3.5). In Fig. 9 the 3D simulation results for different operating parameters are shown for the regular FCPC® chamber (grid A). In the beginning the sheet deflection due to the Coriolis force is very small. The flow is almost parallel to the walls of the inclined chamber. For longer simulation time the deflection increases and the mobile phase sheet hits the chamber wall. This lowers the dispersion and will be counterproductive by means of separation efficiency and the flow pattern becomes more stable.

The effect of the circular flow can also be seen in the simulations. At the chamber entrance the momentum of the circular flow of stationary phase, perpendicular to the flow direction of the mobile phase, is transferred into the mobile phase. Additionally the lower relative velocity between mobile and stationary phase decreases the formation of waves on the surface and oscillations of the sheet. Therefore the sheet break-up is lowered after a short period of simulation time. The sheet deflection of the simulations increases for higher volume flows and rotational speeds due to the higher momentum of the circular flow. This behavior was already observed in the experiments.

The main differences between experiments and simulations resulted from the grid cell size because it was chosen relatively large for applying the VOF method. Especially for higher rotational speeds and greater dispersion the resolution of smaller droplets was not possible using the grid cell size mentioned above. For a correct treatment of a droplet at least the value of the indicator function (phase fraction in a cell) in the center grid cell should reach the value of one. This was not the case for all droplets in the simulation. But this effect had little impact on the main flow pattern. Another reason for differences between simulated and experimental flow pattern are the unevenness and macroscopic geometry differences of the chamber geometry. Especially the chamber walls of the FCPC® rotor plate had a relatively rough surface.

4.3. Interfacial area

The interfacial area for mass transfer IA (see Eq. (9)) is affected by operating parameters and phase properties. The values of the IA should be seen on a qualitative scale because the grid size was not sufficient for a resolution of the smallest droplets. Although the IA is probably slightly overestimated we showed that increasing the grid size had no significant effect on the calculated IA (see Section 3.5). The IA is used for the comparison of different chamber depths and physical properties.

The parameters investigated were the chamber depth, interfacial tension, viscosity ratio and density difference. For the comparison of different chamber depths the specific interfacial area ia was calculated by dividing the interfacial IA through the chamber volume which is 0.129 ml for a chamber depth of 2.5 mm. The results for ia for four different chamber depths are shown in Fig. 10. The results indicate that a greater chamber depth enhanced the specific interfacial area and thus mass transfer and separation efficiency. The trend of the ia corresponds also with the visual observations of the simulated flow pattern. For greater chamber depths the flow was much more dispersed. The increased dispersion resulted from hydraulic diameter of the chamber or higher volume to wall area respectively. Especially the velocities in the chambers in z-direction were increased. This behavior allows an easy scale of CPC devices as already suggested in a patent of Foucault et al. [17].

For estimation of the influence of physical properties on the interfacial area IA six artificial solvent systems, based on the EtAcWat system, were created (see Table 3). The density and dynamic viscosity of the upper phase were set constant whereas interfacial tension, density and viscosity of the lower phase were varied. Additionally the ratio of interfacial tension and density difference is included in the table. This parameter was proven useful by Foucault et al. [18] and our own studies [6] to estimate the stability or the stationary phase retention respectively of a solvent system. The simulations were carried out in grid A (2.5 mm chamber depth), a rotational speed of 1400 rev/min, a volume flow of 15 ml/min and in descending mode (lower phase mobile).
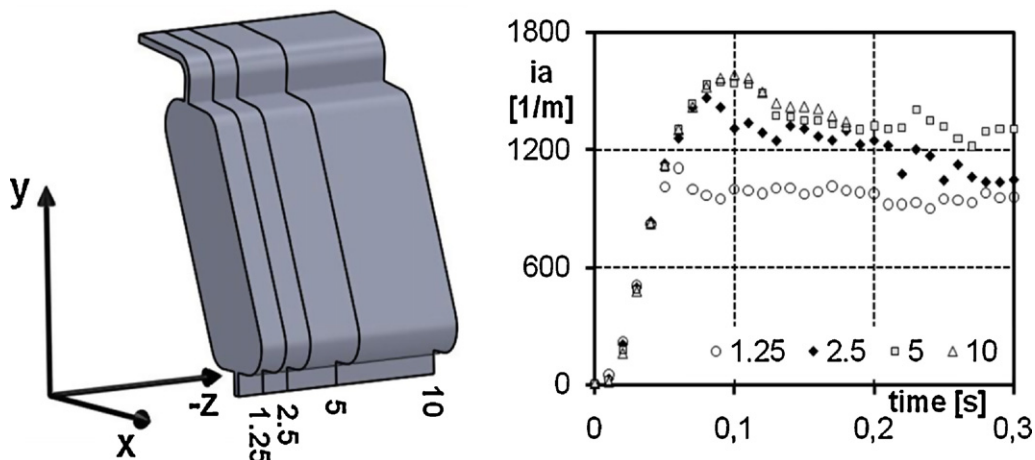
Fig. 10. Influence of chamber depth on specific interfacial area for EtAcWat system (volume flow is 20 ml/min per 2.5 mm chamber depth, rotational speed is 1400 rev/min): simulated chamber depths 1.25, 2.5, 5 and 10 mm with cell counts in z-direction of 15, 30, 60 and 120 and 16,099 cells in xy-plane (left), trend of specific interfacial area for chambers with different depths of 1.25, 2.5, 5 and 10 mm.

The interfacial tension had the strongest influence on the interfacial area IA. Decreasing the interfacial tension (Artificial 1) nearly doubled the interfacial area calculated (see Fig. 11). The flow pattern is more disperse and smaller droplets are formed which causes the enhancement of IA. But the parameter $\sigma/\Delta\rho$ is very small for the Artificial 1 system and a solvent system with similar properties is expected to have lower retention of the stationary phase.

Increasing the density difference had the same effect like decreasing the interfacial tension (see Fig. 12). The flow was more disperse due to the higher velocities and the interfacial area increased. The Coriolis force has a stronger effect on the mobile phase if the density difference is low. Therefore sheet deflection was higher for the lower density difference system (Artificial 3) and the sheet hits the chamber wall earlier.

The viscosity ratio had a comparably small effect on the interfacial area (see Fig. 13). Although the viscosity in the Artificial 6 system was nearly five times higher than in the original one the interfacial area increased only 10–20%. Nevertheless, the higher viscosity of the mobile phase lowers the dispersion and the sheet of mobile phase is more stable. Solvent systems with a high viscosity ratio can be operated at higher volume flows compared to systems with equal viscosities.
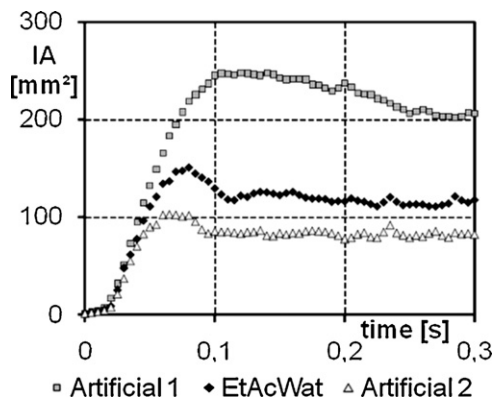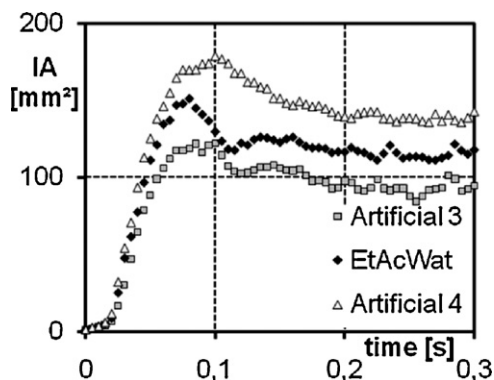

Fig. 12. Trend of interfacial area for different density differences, grid A with 16,099 cells in xy-plane and 30 cells in z-direction is used.
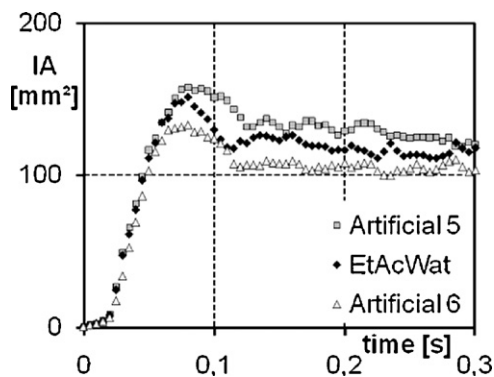

Fig. 13. Trend of interfacial area for different lower phase viscosities, grid A with 16,099 cells in xy-plane and 30 cells in z-direction is used.

5. Conclusions

In this study a three-dimensional CFD model was presented that allows the calculation of the flow pattern in a CPC chamber. The model is based on the VOF method and allows calculating the interfacial area. For the calculation operating parameters and physical properties (densities, interfacial tension, viscosities) are only needed. No empirical correlations are used in the model presented. This allows using the model for a priori calculation of the flow pattern for given operating parameters and phase systems.

Fig. 11. Trend of interfacial area for different interfacial tensions; grid A with 16,099 cells in xy-plane and 30 cells in z-direction used.

The model was validated by comparison with experimentally visualized flow patterns and by a qualitative PIV analysis. The simulation results showed similar flow pattern with a comparable degree of dispersion, which is an important parameter for mass transfer between the phases. Also the deflection of the mobile phase due to the Coriolis force was well predicted. The already assumed circular flow of the stationary phase [6] was proven with the PIV analysis. The circular flow was identified as the reason for the stronger deflection of the mobile phase than expected from the Coriolis force alone. In contrast to the experiments three dimensional flow patterns were accessible using the CFD model. Increasing the volume flow enhances the dispersion and leads to unsteady flow pattern that has different velocity profiles in the z-direction of the chamber.

The influence of different parameters on the interfacial area for mass transfer was analysed. We found a positive influence of increasing chamber depth which allows higher velocities in the z-direction. Therefore scale-up is simple if compared to other unit operations like high performance liquid chromatography (HPLC). The qualitative influence of physical properties on the interfacial area was also presented. The interfacial tension and the density difference were proven as the most important properties because they strongly influence the dispersion.

The model gives multiple options for the future. The model supports the choice of reasonable volume flows and rotational speeds for given phase systems. Additionally it provides the possibility to simulate flow pattern in different geometries of CPC chambers and different operating modes.

Nomenclature

$\vec{a}$	centrifugal acceleration, m/s^2
d	diameter, m
f	frequency, 1/s
$\vec{f}_{sf}$	volumetric interfacial force, N/m^3
ia	specific interfacial area, m^2/m^3
IA	interfacial area, m^2
p	pressure, Pa
R	distance to rotation axis, m
t	time, s
U	velocity, m/s
X	specific direction

Greek letters

α	indicator function (phase fraction)
η	dynamic viscosity, m^2/s
ϕ	mass-specific force, m/s^2
κ	curvature of interfacial area, 1/m
ρ	density, kg/m^3
σ	interfacial tension, kg/s^2
ω	angular velocity, 1/s

Subscripts

1	here: lower mobile phase
2	here: upper stationary phase
ce	centrifugal
Co	Coriolis
gc	grid cell
gr	gravitational
i	control variable
in	inlet
lp	lower phase
out	outlet
p	particle
rel	relative
s	stationary phase
sf	surface
up	upper phase
x, y, z	coordinates

References

[1] C. Roullier, M. Chollet-Krugler, A. Bernard, J. Boustie, J. Chromatogr. B: Anal. Technol. Biomed. Life Sci. 877 (2009) 2067.
[2] A. Berthod, J. Chromatogr. A 1126 (2006) 347.
[3] M.J. van Buel, F.E.D. van Halsema, L.A.M. van der Wielen, K.C.A.M. Luyben, AIChE J. 44 (1998) 1356.
[4] L. Marchal, A. Foucault, G. Patissier, J.M. Rosant, J. Legrand, J. Chromatogr. A 869 (2000) 339.
[5] L. Marchal, J. Legrand, A. Foucault, AIChE J. 48 (2002) 1692.
[6] S. Adelmann, G. Schembecker, J. Chromatogr. A 1218 (2011) 5401.
[7] C.S. Konig, I.A. Sutherland, J. Chromatogr. A 1151 (2007) 131.
[8] Y. Ito, M. Weinstein, I. Aoki, R. Harada, E. Kimura, K. Nunogaki, Nature 212 (1966) 985.
[9] C. Tropea, J. Foss, A.E. Yarin, Handbook of Experimental Fluid Mechanics, Springer-Verlag, Berlin/Heidelberg, 2007.
[10] M. Stiess, Mechanische Verfahrenstechnik, Springer-Verlag, Berlin, 1994.
[11] OpenCFD Limited (Ed.), OpenFOAM. The Open Source CFD Toolbox. User Guide. 1.6. OpenCFD Limited, 24th July 2009.
[12] C.W. Hirt, B.D. Nichols, J. Comput. Phys. 39 (1981) 201.
[13] E. Laurien, H. Oertel Jr., Numerische Stroemungsmechanik, Vieweg/Teubner Verlag, Wiesbaden, 2009.
[14] H. Rusche, Computational Fluid Dynamics of Dispersed Two-Phase Flows at High Phase Fractions (Thesis), Imperial College, University of London, London, 2002.
[15] J.U. Brackbill, D.B. Kothe, C. Zemach, J. Comput. Phys. 100 (1992) 335.
[16] H.J. Ferzinger, M. Perić, Computational Methods for Fluid Dynamics, Springer-Verlag, Berlin, 1997.
[17] A. Foucault, J. Legrand, L. Marchal, D. Durand, Patent US 2008/003546 A1.
[18] A.P. Foucault, E.C. Frias, C.G. Bordier, F. Legoffic, J. Liq. Chromatogr. 17 (1994) 1.